Investigation of an alternate computationally efficient technique to model laser shock peening by modification of the pressure load

Jacques Karel Dreyer[1, a *], Dawood Ahmed Desai[1, b] and Schalk Kok[2, c]

[1]Department of Mechanical and Mechatronics Engineering, Faculty of Engineering and the Built Environment, Tshwane University of Technology, South Africa

[2]Department of Mechanical and Aeronautical Engineering, Faculty of Engineering, Built Environment and Information Technology, University of Pretoria, South Africa

[a]jacqueskdreyer@gmail.com, [b]desaida@tut.ac.za, [c]schalk.kok@up.ac.za

Keywords: Laser shock peening, pressure load, quasi-static analysis, explicit analysis.

Abstract. Appropriate computational techniques to model laser shock peening to retrieve residual stress results using finite element modelling are largely under investigation. Hence, this original study investigated a numerical modelling technique employing a quasi-static analysis (using ABAQUS CAE) to deliberately introduce approximation into the analysis by ignoring the inertia normally present in a conventional dynamic explicit laser shock peening analysis (which has good prediction capability of residual stresses) in order to reduce computational time. To compensate for the modelling approximation, the input pressure load spatial profile parameters were varied in an attempt to obtain similar surface residual stress results to those of a dynamic explicit analysis. Such a study has not previously been conducted.

The outcome of the study showed that a quasi-static analysis accelerates the simulation time up to 29 times. In addition, when machine learning with a partial least squares algorithm (employing the PyCharm Python integrated development environment) was used on the quasi-static input spatial profile and output surface residual stress data sets (obtained from performing trial and error in order to match the dynamic explicit results closely), the quasi-static input spatial results were obtained in sub one second, aiding with computational efficiency. Applying the predicted profile to the quasi-static model resulted in the surface residual stress profiles correlating well for the first 0.5 mm, with a 7.88% difference to the dynamic explicit model and a 3.27% difference to the experimental result. However, this explorative study demonstrated that the quasi-static modelling technique produced unrealistic results when the other principal stress components are compared to the dynamic explicit model. It becomes clear that inertial effects are essential in modelling laser shock peening realistically. Therefore, when stress components other than the surface residual stress profile in one plane are required, the conventional dynamic explicit analysis technique should be employed.

Introduction

Numerous studies in recent years have been conducted on the improvement of fatigue life in metals through applying surface improvement technologies. The solution to the problem at hand is metallic surface enhancement processes like laser shock peening (LSP), shot peening (SP), ultrasonic nanocrystal surface modification (UNSM) and cavitation shotless peening (CSP). The LSP process proved its advantages resulting in a deeper compressive residual stress and a smoother surface finish compared to the other surface improvement technologies [1-3]. LSP was first commercially applied in the early 1990s, more than 20 years after it was developed, in the aviation industry when members of the United States Air Force realized that the turbine blades used on the B-1B bomber aircraft had a significantly longer blade-life when LSP was applied to it [4]. The success in the aviation industry turned to the power generation industry in 2009 when the LSP process was first applied on steam turbine components [5]. To reduce the failure from fatigue in steam turbine blades, laser peening is used to enhance the properties of the 12% Cr FV-566 martensitic stainless steel material used on these blades.

Fig. 1 illustrates the LSP process. LSP is performed by firing a high-intensity laser onto a water-confined, opaque ablative layer applied to the target surface of the material. This results in a plasma formation on the surface which causes a shock wave to form and propagate through the target material, resulting in induced compressive stresses within the material, and by extension, increased damage tolerance and fatigue life.

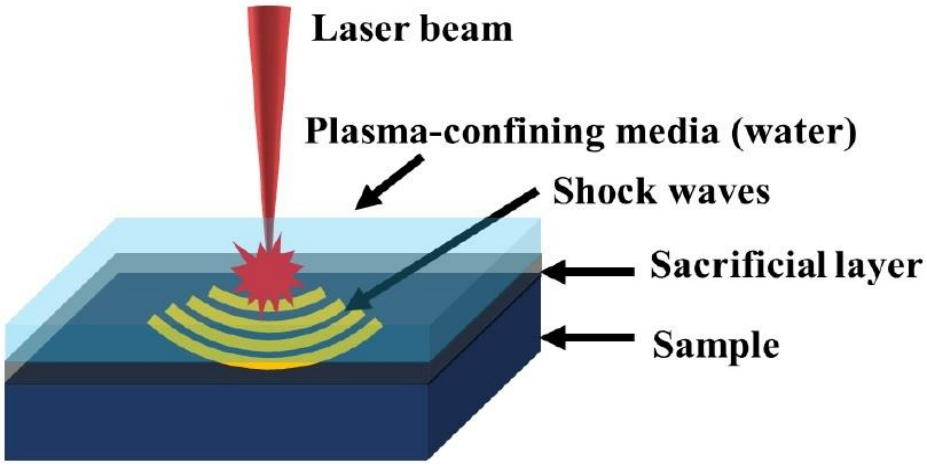

Fig. 1. LSP schematic [1]

There is an increasing demand for simulation techniques to be developed to enable minimization of the modelling effort for ultimately a more efficient numerical model. There are currently two prominent techniques used for performing simulations on LSP namely the full explicit-explicit method where all the steps are full dynamic explicit and then the explicit-standard, where the impact step is explicit and the relaxation step is performed in standard [6]. Hence this study attempts to develop a full standard technique for the impact step employing a 2D axisymmetric model. For surface residual stress comparison purposes, a study by Armfield [7] successfully predicted surface residual stress utilizing a 2D axisymmetric model with a full explicit analysis and experimental results by the National Laser Centre (NLC) division at the Council for Scientific and Industrial Research (CSIR) were available in literature.

The study attempts to assist engineers working in the power generation industry, by developing a technique that can be implemented by them to simulate the LSP process and avoiding lengthy and expensive processes corresponding with X-ray diffraction (XRD) testing to retrieve residual stress surface plots [8]. The investigative research seeks to provide a more efficient numerical method of simulating the LSP process, without ignoring any important factors that contribute to a realistic simulation result.

Finite element modeling

LSP simulation procedure. In order to compare the LSP process in FEA to an actual peened sample, a 2D axisymmetric model was created in ABAQUS CAE 2017 (a 2D axisymmetric model is a model revolving around an axis, representing a 3D model). Axisymmetric models are smaller in size relative to 3D models, thus allowing for a full relaxation step to be included in the dynamic explicit analysis and resulting in shorter computational time. The 2D axisymmetric models are a realistic representation of the actual LSP component and residual stress results can be obtained much faster [8,9]. In a study by [10], a full 3D analysis run time in ABAQUS is compared to a 2D axisymmetric model with the same input parameters, when 4 laser shots are applied to the target surface of both models the 3D model takes up to 30 times longer to compute.

Two-step definitions were selected for the dynamic explicit simulation namely a dynamic explicit impact step of 2.5×10^{-7} seconds followed by a dynamic explicit relaxation step (where the

material achieves static equilibrium after the dynamic effect of the impact step), totalling the simulation time to $1x10^{-4}$ seconds. Whereas in the quasi-static analysis a single step definition was selected because no relaxation takes place in a standard static step. A static general impact step of $2.0x10^{-7}$ seconds was selected at which point the impact temporal load has reduced to zero, refer to Fig. 3. The boundary conditions used for the 2D axisymmetric model has a zero displacement in the y- and x-direction and a zero angular displacement about the z-axis, which is applied to the bottom elements of the model (relative to Fig. 4). This allows for wave propagation through the boundaries replicating the actual fixed shock peened component in industry.

Mesh design. The two different sections of the model (the 1mm wide far-field section) uses axisymmetric infinite elements (CINAX4). This allows wave propagation through the boundary (instead of wave reflections). Fig. 2 illustrates the final mesh design with smaller elements closer to the impact area and a 45-degree element angle at the bottom right corner to allow waves to pass through the edge of the model. The 5 mm by 10 mm solid body (the same thickness as the experimental peened block and width much larger than the laser spot to ensure residual stresses imparted in the model is far from the outer edges) employs CAX4RT elements the same as Armfield [7]. The total number of elements combining the two sections is 3603.

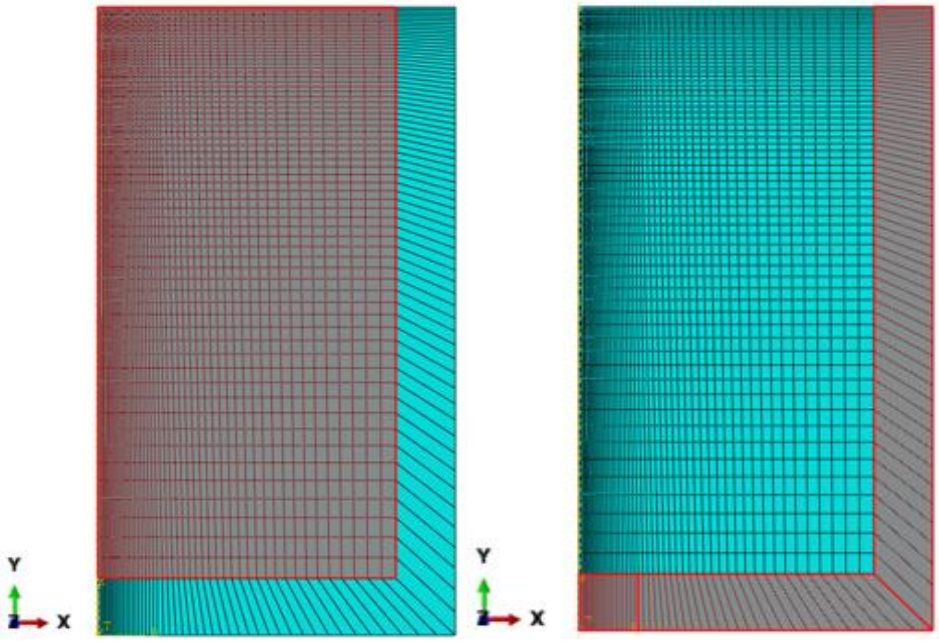

Fig. 2. Mesh design solid section (left) infinite section (right)

Material model and material properties. The LSP process has been found to cause very high strain rates of over 10^6 s^{-1} to occur in the target material which causes permanent microstructural changes near the material surface [11,12]. There exist several material constitutive laws that allow for numerical characterisation of the behaviour of the material at high strain rate conditions. However, the preferred physics-based material model employed in the study is the mechanical threshold stress (MTS) method over the well-known Johnson-Cook method since the MTS method is capable of predicting more accurate strain-rate-dependent residual stress predictions compared to the Johnson-Cook method [7].

The MTS method describes the strain-rate-dependent plastic behaviour of the target material [13-15]. The mechanical threshold $\hat{\sigma}$ has a theoretical maximum at 0 K and can be expressed as follows:

$$\hat{\sigma} = \hat{\sigma}_a + \sum_K \hat{\sigma}_t^K \quad (1)$$

where $\hat{\sigma}_a$ is the athermal stress component and $\hat{\sigma}_t^K$ denotes the thermal components where $K = 1$ and $K = 2$ represent the non-evolving and the evolving thermal component respectively.

The thermal components of the mechanical threshold are scaled by scaling factors for $K = 1$ and $K = 2$. The scaling factors are functions of plastic strain rate and temperature and are indicated by:

$$S_t^K(\dot{\varepsilon},T) = \left[1 - \left(\frac{kT}{g_{0t}^K \mu b^3} \ln \frac{\dot{\varepsilon}_{0t}^K}{\dot{\varepsilon}}\right)^{\frac{1}{q_t^K}}\right]^{\frac{1}{p_t^K}} \tag{2}$$

where g_0 is the normalised activation energy; k is the Boltzmann constant; b is the Burger's vector of the target material; and $\dot{\varepsilon}$ is the plastic strain rate. The relationship between k, g_0 and b can be reduced to form a new constant a_{0t}^K that is expressed as follows:

$$a_{0t}^K = \frac{g_{0t}^K b^3}{k} \tag{3}$$

The MTS is now scaled to the flow stress σ_y using the relationship:

$$\frac{\sigma_y}{\mu} = \frac{\hat{\sigma}_a}{\mu} + \sum_K S_t^K(\dot{\varepsilon},T) \frac{\hat{\sigma}_t^K}{\mu_0} \tag{4}$$

Here, μ_0 is the shear modulus at 0 K and 0 Pa (0 pressure) [13]. If there are two thermal components, one evolving and one non-evolving, Eq. 4 becomes:

$$\frac{\sigma_y}{\mu} = \frac{\hat{\sigma}_a}{\mu} + S_i(\dot{\varepsilon},T) \frac{\hat{\sigma}_i}{\mu_0} + S_\varepsilon(\dot{\varepsilon},T) \frac{\hat{\sigma}_\varepsilon}{\mu_0} \tag{5}$$

where $\hat{\sigma}_i$ is the yield stress thermal portion (the non-evolving thermal stress component) and $\hat{\sigma}_\varepsilon$ is the evolving thermal stress component. The evolution of $\hat{\sigma}_\varepsilon$ in rate form is given by the expression:

$$\frac{d\hat{\sigma}_\varepsilon}{d\varepsilon} = \theta(\hat{\sigma}_\varepsilon,\dot{\varepsilon},T) = \theta_0 - \theta_r(\hat{\sigma}_\varepsilon,\dot{\varepsilon},T) \tag{6}$$

where θ_0 is an assumed constant representing the hardening due to dislocation build-up; θ_r is the dynamic recovery rate; and θ the hardening rate. The hardening rate can be expressed in tanh form as follows:

$$\theta = \theta_0 \left(1 - \frac{\tanh\left(\frac{\alpha\hat{\sigma}_\varepsilon}{\hat{\sigma}_{\varepsilon s}}\right)}{\tanh(\alpha)}\right) \tag{7}$$

where $\hat{\sigma}_{\varepsilon s}$ is the saturation threshold stress.

The shear modulus μ is temperature dependant and is computed from the empirical relationship

$$\mu(T) = \mu_0 - \frac{D_0}{exp\left(\frac{T_0}{T}\right) - 1} \quad (8)$$

where D_0 and T_0 are empirical constants (here T_0 was selected as a reference temperature of 208 K). According to [15,16], the material response is insensitive to the reference strain rates $\dot{\varepsilon}_{0e}$ and $\dot{\varepsilon}_{0es}$ and, therefore, remains constant at 10^7 s^{-1}. The remaining MTS constants are tabulated in Table 2.

Performing tests with a Gleeble thermal-mechanical simulator on the 12% Cr FV-566 steam turbine blade test samples, the MTS material model parameters were calibrated experimentally and optimized by Armfield [7]. Table 1 and Table 2 shows the mechanical properties of FV-566 and the calibrated MTS material model parameters respectively [7].

Table 1. Mechanical material properties of 12% Cr FV-566 [7]

Property	Units	Value
Density	Kg/m^3	7758
Young's modulus	GPa	168.95
Poisson's ratio		0.3
Bulk modulus	GPa	140.79
Shear modulus	GPa	64.98
Specific heat	J/kg.K	490

Table 2. MTS material model parameters [7]

Property	Units	FV-566 (12% Cr) stainless-steel
Reference shear modulus (μ_0)	GPa	71.48
Material constant (D_0)	GPa	8.64
Reference temperature (T_0)	K	208
Poisson's ratio (ν)		0.3
Athermal stress component (σ_a)	MPa	0
Evolving stress component (σ_{E0s})	MPa	1767.5
Non-evolving stress component (σ_i)	MPa	2193.02
Normalized activation energy due to dislocation-dislocation interactions (g_{E0})	K/MPa	7.82
Activation energy (g_{E0s})	K/MPa	4.232
Normalized activation energy (g_{0i})	K/MPa	1.48
Strain hardening rate (θ_0)	MPa	9183.62
Reference strain rate (ε_0)	s^{-1}	$1E^7$
Maximum strain rate (ε_{E0s})	s^{-1}	$1E^7$
Constant MTS parameter (q_e)		1
Constant MTS parameter (p_e)		0.667
Constant MTS parameter (q_i)		1.5

Constant MTS parameter (p_i)		0.5
Hardening constant (α)		2.3

Pressure pulse loading. The plasma pressure exerted on the surface of the peened part follows a temporal (duration and shape) profile which describes the pressure-time history over the analysis step time [17]. The short-rise-time (SRT) pressure temporal loading profile illustrated in Fig. 3 is the profile adopted by [7] from a study with a similar LSP setup [18] to the experimental peened samples from the CSIR NLC. All ABAQUS explicit dynamic and standard quasi-static simulation models used this profile trailing off to zero at 2.0×10^{-7} seconds. Fig. 4 depicts the spatial pressure loading profile on the target material which is non-uniformly distributed and assumed to be spherical. In this study the spatial profile undergoes modification and by utilizing the analytical mapping feature in ABAQUS it allows an unlimited amount of different shapes and sizes of spatial pressure profiles to be applied to the surface of the model. This feature leads to a more realistic residual stress prediction from the numerical solver.

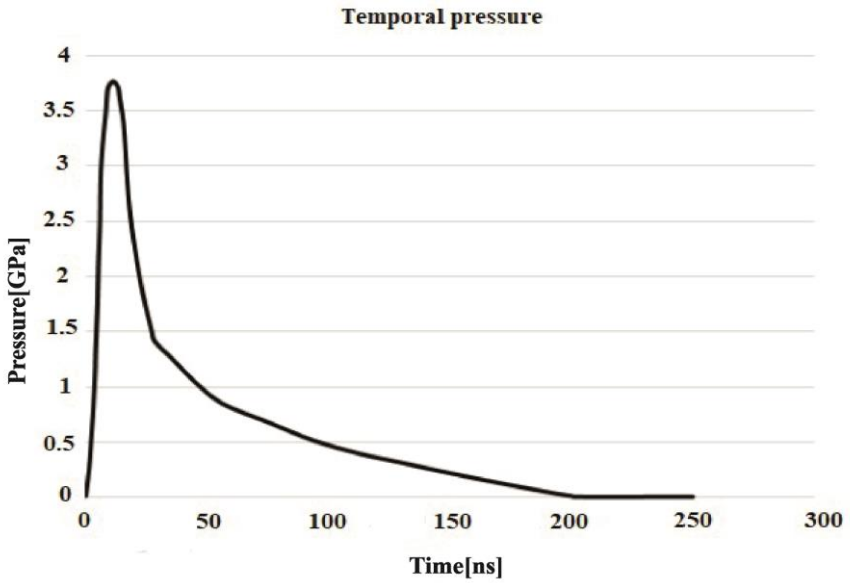

Fig. 3. Temporal loading pressure profile [7]

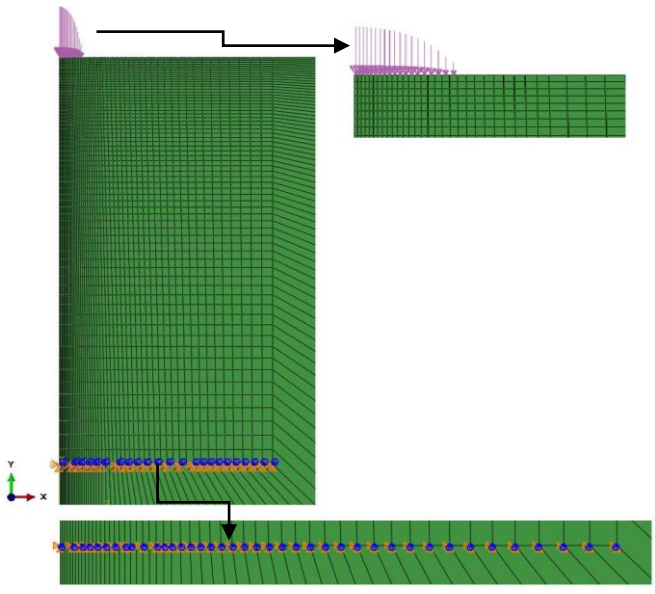

Fig. 4. Spatial loading pressure profile

The peak applied pressure is calculated using Eq. 9 (when water is the overlay medium) described by [8]:

$$P = 0.01\sqrt{\frac{\alpha_{eff}}{2\alpha + 3}}\sqrt{Z}\sqrt{I_0} \tag{9}$$

where P is the peak pressure load in GPa; α_{eff} is the efficiency of the laser interaction; Z is the shock impedance between the material and the water overlay medium measured in g/cm^{2}s^2; and I_0 is the laser power density in GW/cm^2. The shock impedance between the material and overlay medium is defined by Eq. 10:

$$\frac{2}{Z} = \frac{1}{Z_{target\ material}} + \frac{1}{Z_{water}} \tag{10}$$

where $Z_{target\ material}$ is the shock impedance of 12% Cr FV-566 and Z_{water} is the shock impedance of the water overlay.

Taking the shock impedance of water and FV-566 to be 0.165 MPa.s/m and 51.8 MPa.s/m respectively and the interaction efficiency to be 0.3 [7]. The peak pressure was calculated to be 3.79 GPa for a 5.25 GW/cm^2 laser shot.

Results

Dynamic explicit model. For comparison purposes, a single 5.25 GW/cm^2 laser pulse was applied to the surface of the model employing the ABAQUS explicit-explicit method.

Fig. 5 (left) displays the S11 residual stress result from Armfield [7]. Fig. 5 (right) displays the dynamic explicit replicated result.

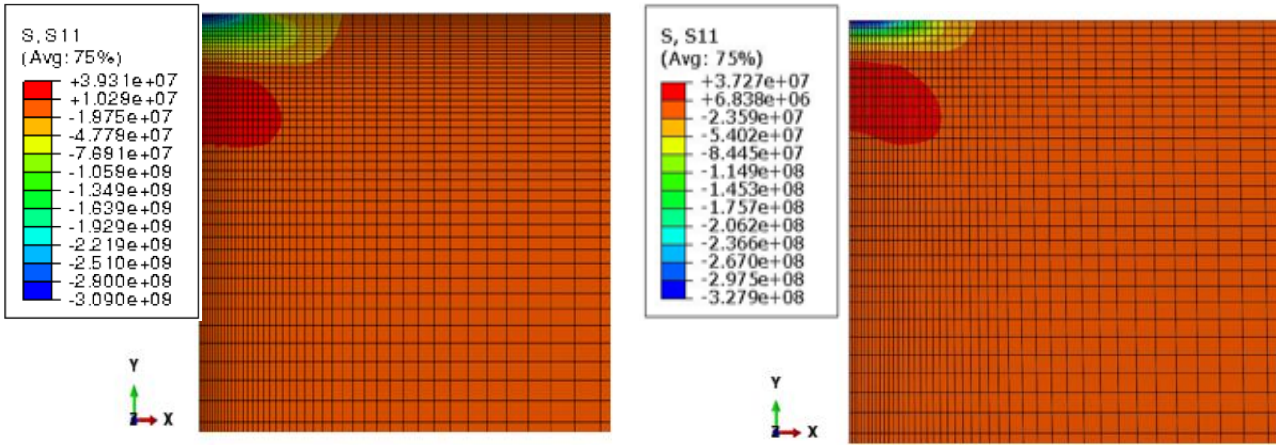

Fig. 5. S11 dynamic explicit Armfield [7] (left) vs. S11 dynamic explicit replicated (right)

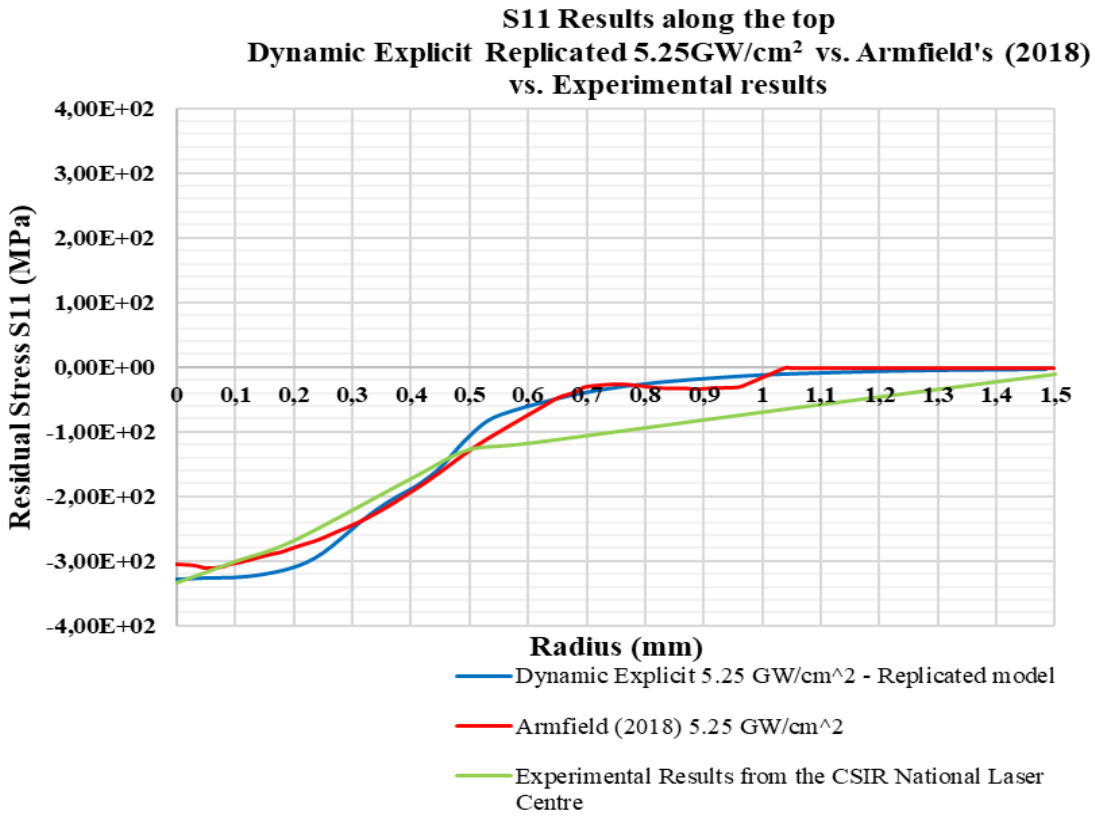

Fig. 6. S11 replicated vs. Armfield [7] vs. experimental result

Fig. 6 presents the comparison of S11 surface residual stresses between the replicated dynamic explicit model, Armfield's [7] model and the experimental results from the CSIR NLC. Since both the replicated model and Armfield's [7] model use the same material subroutine, the difference can only be attributed to different mesh refinement. Table 3 illustrates the variance between Armfield's [7] model and the replicated dynamic explicit model.

Table 3. Armfield (2018) vs. dynamic explicit results

Armfield (2018) residual stress (stress in the radial direction), S11 (MPa)	**Replicated dynamic explicit residual stress (stress in the radial direction), S11 (MPa)**	**Variance = [Armfield (2018)] – [Dynamic explicit] / [Armfield (2018)] (%)**
39.31	37.27	5.1
-309	-327.9	5.7
Armfield (2018) stress in the axial direction, S22 (MPa)	**Replicated dynamic explicit stress in the axial direction, S22 (MPa)**	**Variance = [Armfield (2018)] – [Dynamic explicit] / [Armfield (2018)] (%)**
58.45	60.38	3.1
-18.66	-18.02	3.4
Armfield (2018) hoop direct stress, S33 (MPa)	**Replicated dynamic explicit hoop direct stress, S33 (MPa)**	**Variance = [Armfield (2018)] – [Dynamic explicit] / [Armfield (2018)] (%)**
39.21	37.79	3.6
-306.5	-329.1	6.8

Armfield (2018) shear stress, S12 (MPa)	Replicated dynamic explicit shear stress, S12 (MPa)	Variance = [Armfield (2018)] – [Dynamic explicit] / [Armfield (2018)] (%)
28.25	29.69	4.8
-9.86	-9.301	5.6

Quasi-static model. After successfully replicating the dynamic explicit model, the analysis type was changed to quasi-static. Thus, employing the identical model geometry, boundary conditions, pressure load intensity, etc. Only the dynamics was omitted and the MTS VUHARD subroutine [7] was replaced by the MTS UHARD subroutine [15].

Fig. 7 depicts the S11 surface residual stress after the load had reduced to 0 for the dynamic explicit vs. the quasi-static analysis.

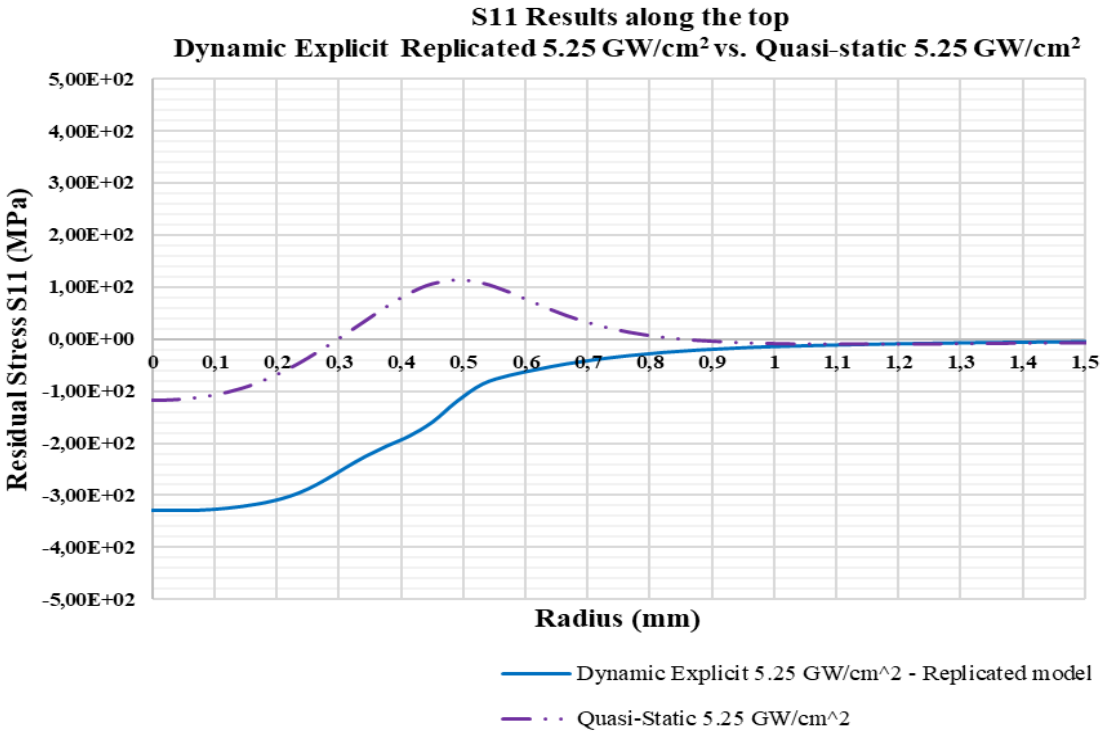

Fig. 7. Dynamic explicit vs. quasi-static results with the same laser intensity

From Fig. 7 it was clear that the laser intensity and the radius of the pressure load needed to increase to obtain closer surface residual stress results to that of the dynamic model.

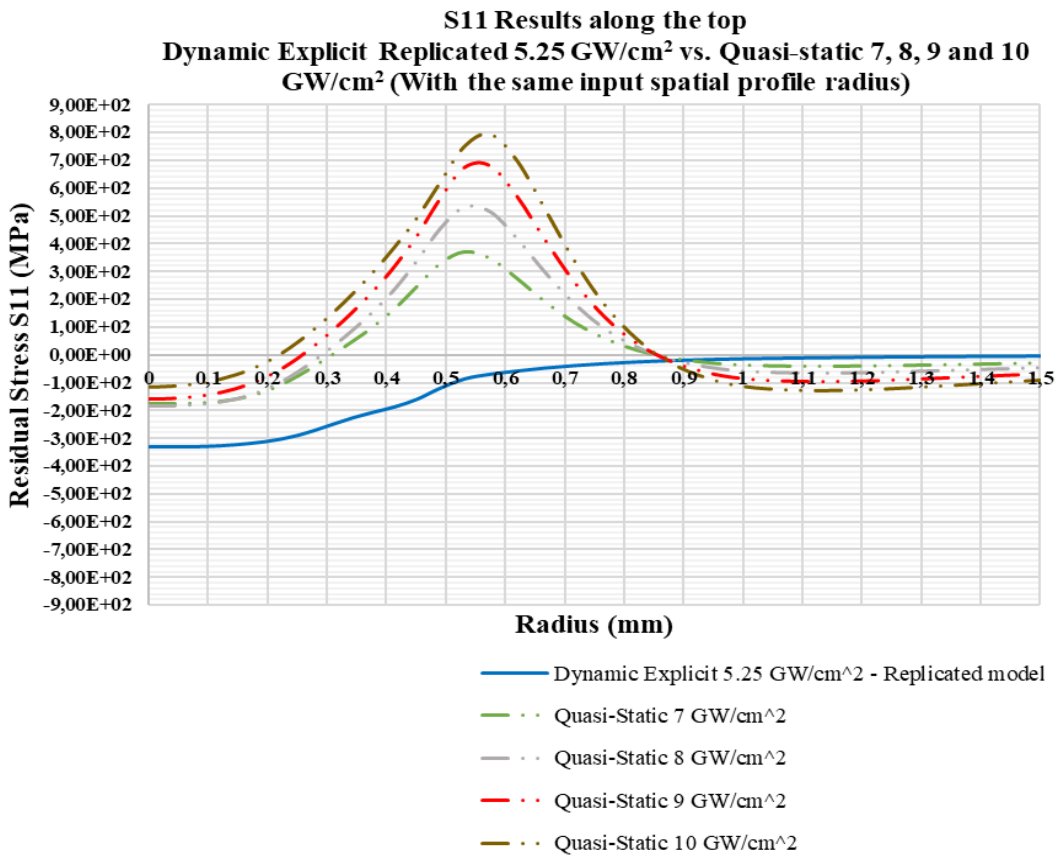

Fig. 8. Dynamic explicit vs. quasi-static results with increased laser intensity

Fig. 8 demonstrates that by only increasing the laser intensity, the explicit results cannot be matched. Instead, the impact load radius can be increased.

The increased radius demonstrated that the part of the curve previously in the tensile region was decreased to the compressive region and closer to the dynamic explicit result refer to Fig. 9. The quasi-static simulation with the 10 GW/cm^2 and 2.5 mm radius were selected for further spatial profile modification.

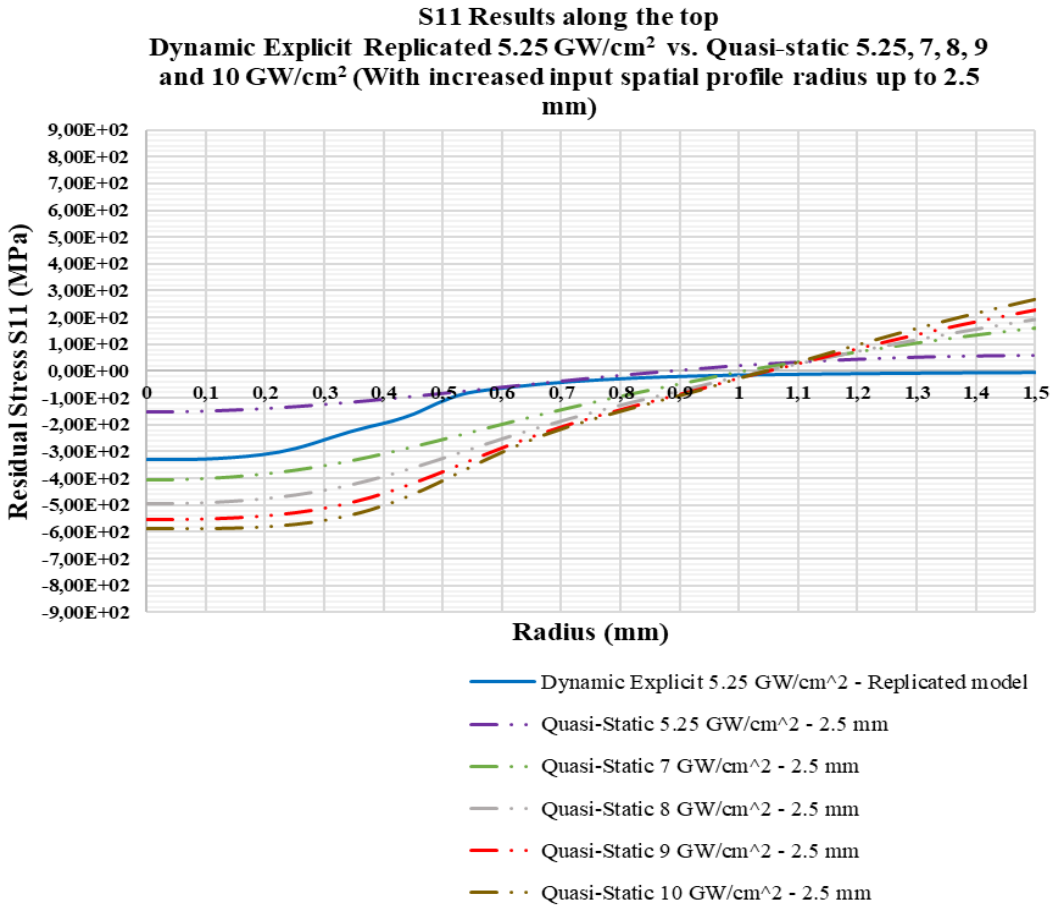

Fig. 9. Dynamic explicit vs. quasi-static for impact radius 2.5 mm

Computational saving. The dynamic explicit and quasi-static simulation times (Real analysis times) for a single laser shot are presented in Table 4. The quasi-static model revealed a computational saving of 96%, increasing the total job run time by ±29 times.

Table 4. ABAQUS job duration

Job duration ABAQUS	**Dynamic explicit simulation time**	**Quasi-static standard simulation time**
Real analysis / computational time (seconds)	1583	55

Machine learning. Machine learning is a broadly used method to make predictions in data science, engineering and statistics [19]. Machine learning is a fast and efficient method of obtaining a relationship between input and output data sets. Numerous different input shapes with different radiuses were applied to the quasi-static model to attempt to get close results to that of the dynamic explicit analysis, thus resulting in large data sets of input and output coordinates. Partial least squares (PLS) is a linear mapping tool between two high dimensional data sets. The PLS algorithm is used in this study between the input spatial profile coordinates and the output residual stress coordinates. The coordinates are obtained from 50 quasi-static (10 GW/cm^2) trial and error simulations performed to attempt to match the dynamic explicit result as close as possible, refer to Fig. 11. By developing a Python code, it enables a predictive input spatial result (quasi-static) to be generated if applying the dynamic explicit residual stress output result to the code. Fig. 10 shows the input shapes applied to the quasi-static model to attempt to closely match the dynamic model. Fig. 11 show the results of the input shapes applied in Fig. 10 compared to the dynamic explicit result.

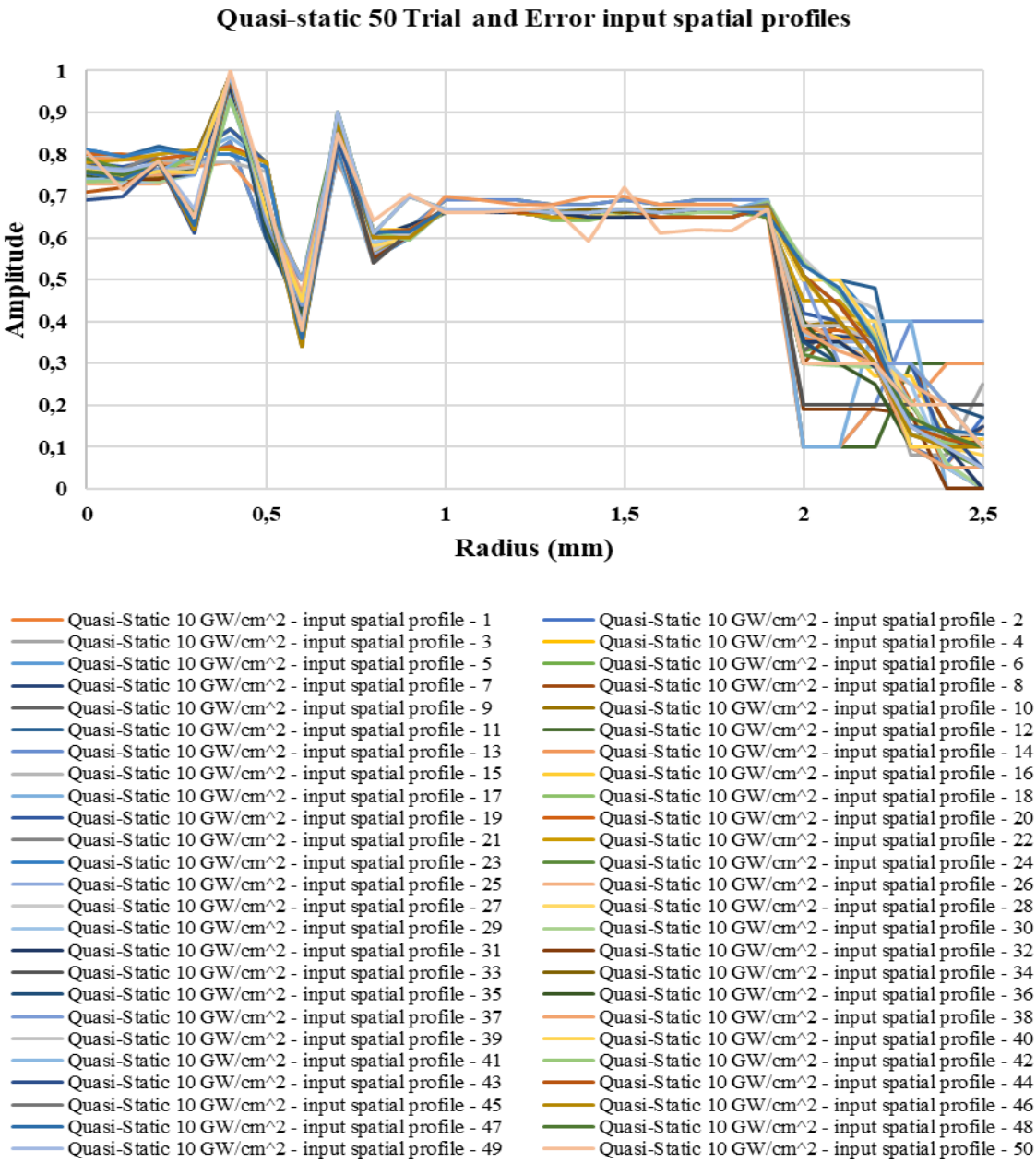

Fig. 10. Fifty quasi-static input spatial profiles

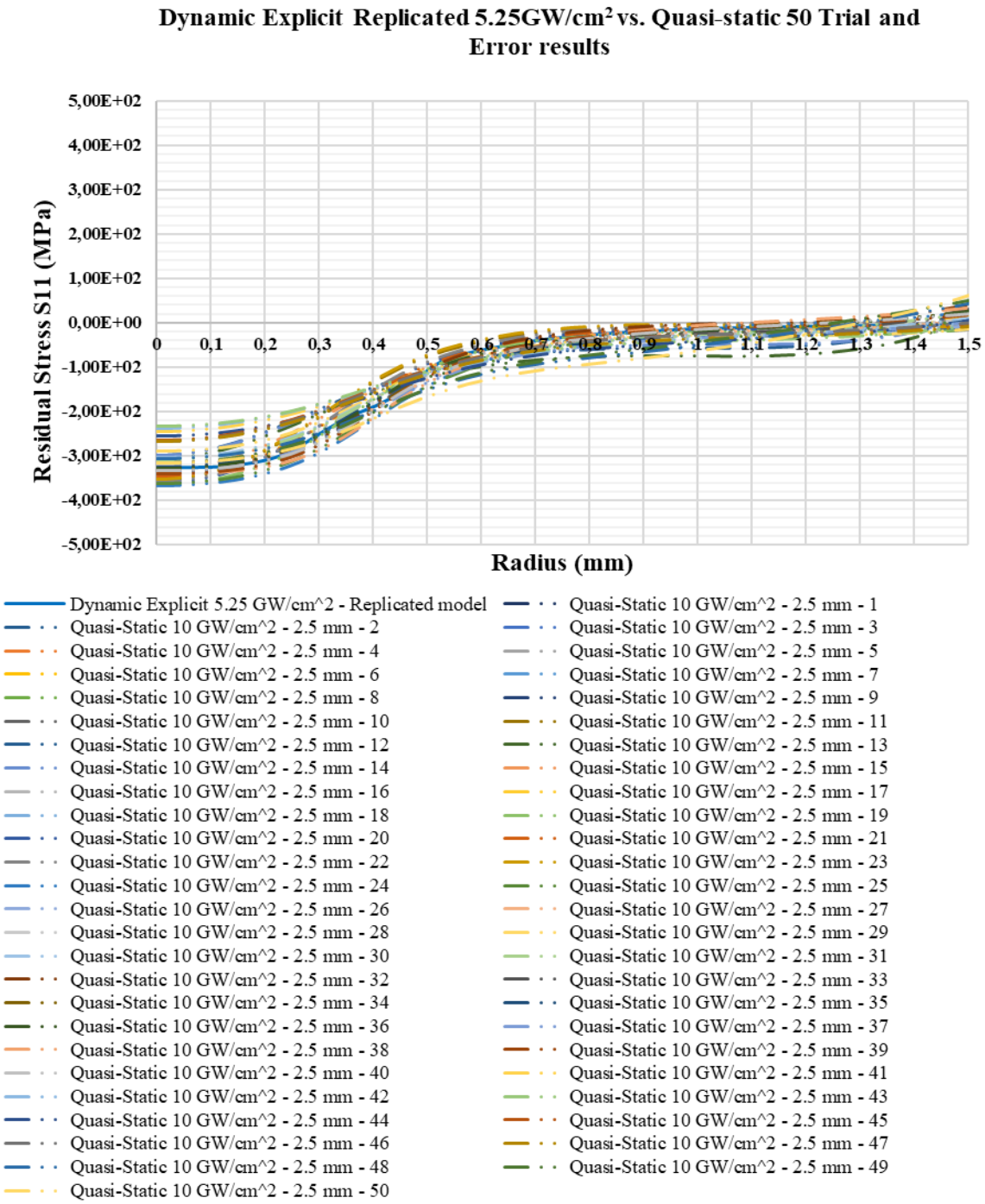

Fig. 11. Dynamic explicit vs. 50 quasi-static trial and error results

Fig. 12 shows the original spatial profile (blue curve) vs. the modified predictive spatial profile (orange curve) in order to match the top surface residual stress for both the dynamic and non-dynamic models.

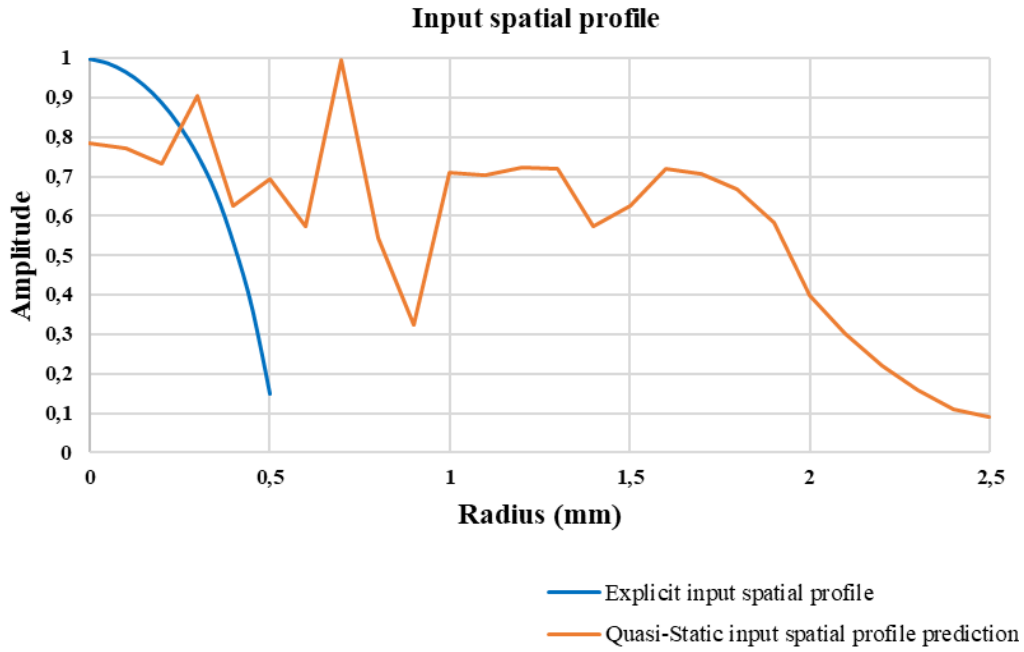

Fig. 12. Input spatial profile comparison

Results comparison. The input spatial prediction result from Fig. 12 was applied to the quasi-static model and produced the result depicted in Fig. 13. Fig. 13 shows the S11 top surface residual stress profile results in which the dynamic explicit replicated model is compared with the quasi-static prediction model, Armfield's [7] model and the results obtained from the CSIR NLC on the peened sample by non-destructive XRD.

Fig. 13 illustrates a reliable surface residual stress result (results of importance in this study) that correlates well with the other curves.

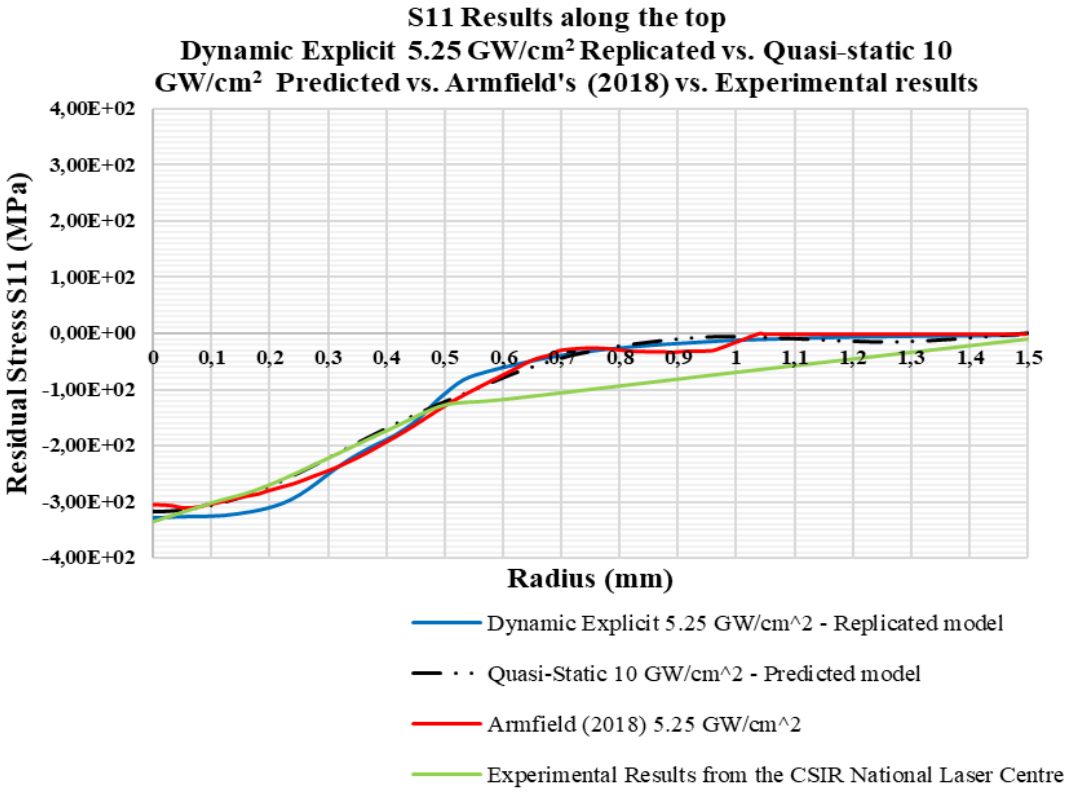

Fig. 13. Dynamic explicit 5.25 GW/cm^2 vs. quasi-static 10 GW/cm^2 vs. Armfield (2018) vs. experimental results

Please note the maximum S11 compressive residual stress (highlighted in blue) is the result of interest in this study and the other principal stress components included in Table 5 is simply to illustrate the large effect of simulating the laser peening process with a non-dynamic simulation on different axes.

Table 5. Quasi-static vs. dynamic explicit results

Quasi-static residual stress (stress in the radial direction), S11 (MPa)	**Replicated dynamic explicit residual stress (stress in the radial direction), S11 (MPa)**	**Variance = [Quasi-static] – [Dynamic explicit] / [Quasi-static] (%)**
454.4	37.27	91.8
-318.01	-327.9	3.0
Quasi-static stress in the axial direction, S22 (MPa)	**Replicated dynamic explicit stress in the axial direction, S22 (MPa)**	**Variance = [Quasi-static] – [Dynamic explicit] / [Quasi-static] (%)**
131.4	60.38	54.05
-151.4	-18.02	88.1
Quasi-static hoop direct stress, S33 (MPa)	**Replicated dynamic explicit hoop direct stress, S33 (MPa)**	**Variance = [Quasi-static] – [Dynamic explicit] / [Quasi-static] (%)**
152.2	37.79	75.17
-318.22	-329.1	3.31
Quasi-static shear stress, S12 (MPa)	**Replicated dynamic explicit shear stress, S12 (MPa)**	**Variance = [Quasi-static] – [Dynamic explicit] / [Quasi-static] (%)**
111.1	29.69	73.27
-73.88	-9.301	87.41

Although the S11 compressive surface profile results appeared promising and practical, when plotting the curve into the depth of the model, the differences in neglecting the inertia effects with the quasi-static model are seen in Fig. 14 and Fig. 15.

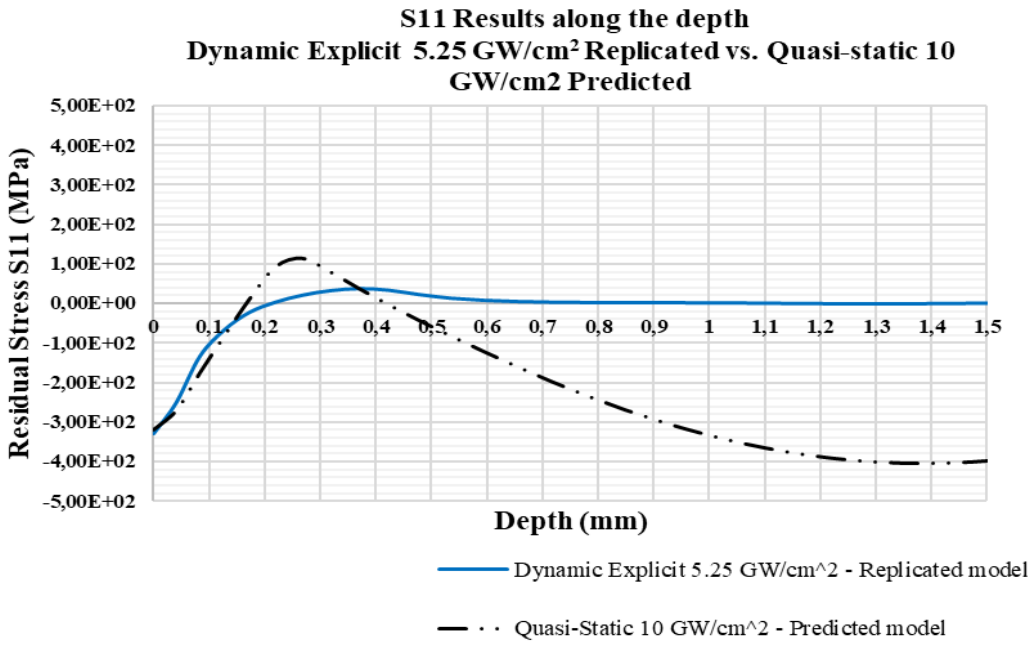

Fig. 14. Dynamic explicit replicated model vs. quasi-static prediction model – S11 results along the depth

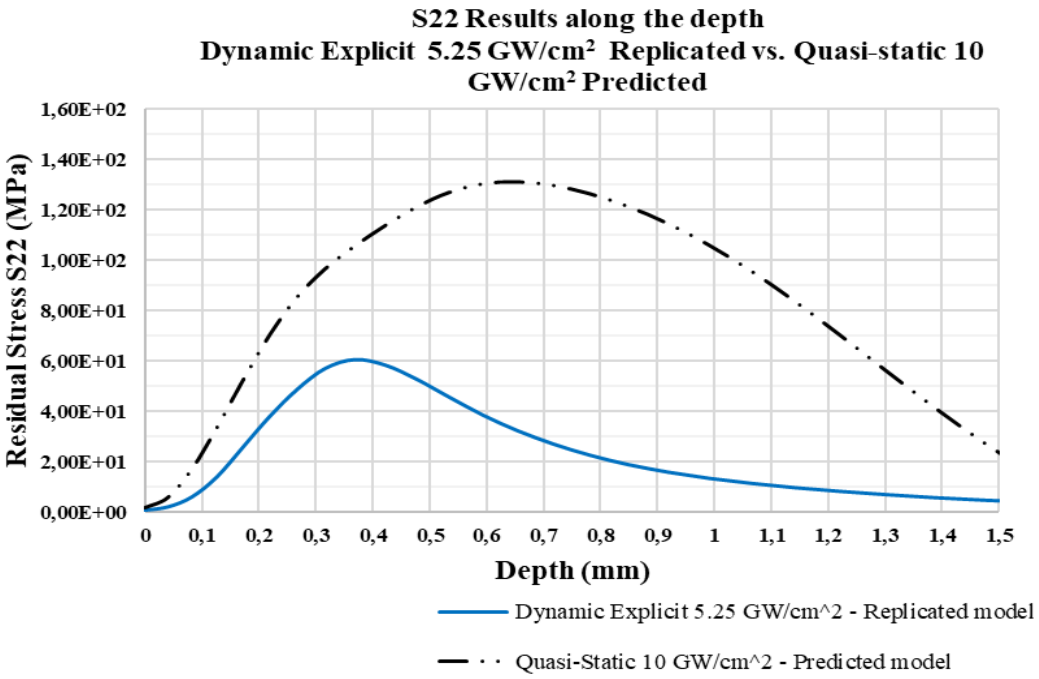

Fig. 15. Dynamic explicit replicated model vs. quasi-static prediction model – S22 results along the depth

Discussion

The outcome of this exploratory study showed that the elastic and plastic shock waves propagating through the target material in LSP must be considered. In addition, it is crucial to model the process numerically in order to obtain a realistic representation of what occurs in the actual LSP event. It was initially anticipated that by neglecting only the dynamics in a laser peening simulation, the results would be acceptable and useable and would be able to improve the LSP simulation regime. However, by matching the S11 compressive surface residual stress profiles, the other stress components when compared, did not match at all. Nevertheless, the S11 component, which is of practical interest, correlated well. Thus, answering the research question through the reported results. The computational time increased by more than 96% for the non-dynamic simulation, agreeing with literature which stated that non-dynamic 2D axisymmetric simulations run faster when the numerical models are smaller in size [10,20].

The study contributed to knowledge by showing that the inertial effects are essential in modelling a realistic LSP process and that conventional explicit-explicit or explicit-implicit models should be employed for residual stress prediction even though the non-dynamic and dynamic profile correlated well. The study also showed that the MTS material model makes realistic predictions in high strain-rate-dependent models such as the LSP event in dynamic explicit FEM which agrees with Munoz [21].

The S11 results into the depth of the model and S22 results shows the changes in the residual stress results even when the top surface S11 residual stress profile is matched.

The 2D axisymmetric model developed in this study confirm the statements made by [8,22]. That 2D axisymmetric models saves computational time without sacrificing the accuracy of the simulation result. Refer back to Fig. 13 for the close correlation between the 2D dynamic model and the CSIR experimental results.

Conclusion

The need for accurate and computationally efficient numerical modelling techniques for LSP is significant. Hence, this study aimed to develop the regime further by modifying parameters on an already computational efficient 2D axisymmetric model and ignoring the dynamics in an attempt to further improve the LSP computational time. In this work, a dynamic explicit model was initially developed and compared with the model of Armfield [7] and the CSIR experimental results in order to establish a trustworthy result and a basis for this study. Thereafter, the numerical model was further developed by modification of the laser input spatial profile size and shape in an attempt to match the dynamic surface residual stress profile. Modification of the input pressure profile was a trial and error process that involved increasing the radius and impact intensity gradually and comparing the different results of the altered load with the successfully replicated results and the CSIR experimental results.

In this research, the possibility of performing a non-dynamic axisymmetric numerical model in an attempt to enhance the LSP simulation regime was investigated, by introducing a computationally efficient technique to model LSP in a quasi-static environment which was never done before. A 96% computational time improvement was made for a single laser shot. Regardless of the success in increasing the computational efficiency and matching the quasi-static S11 surface residual stress profile to that of the dynamic explicit profile, the investigation ended with unrealistic quasi-static results in the remaining principal stress components, with some results being up to 1

order of magnitude larger than that of the realistic dynamic explicit analysis. This displayed the importance of inertial effects in LSP.

From the results, the quasi-static and the dynamic explicit models had a low mean average percentage difference of 3.27% and 7.47% when compared with the CSIR experimental results, while Armfield's model [7] had a mean average percentage difference of 6.41% when compared to the CSIR experimental results.

Therefore, in contribution to the LSP simulation regime, it can be stated that if you are interested in all the principal stress results the conventional dynamic explicit technique should be used. However, the surface residual stress was matched, the results compared and what was aimed for in this investigative study was achieved.

Acknowledgements

This research has been supported by the Tshwane University of Technology (TUT) and the University of Pretoria (UP), South Africa. The support from the Eskom Power Plant Engineering Institute (EPPEI), South Africa is appreciated.

Declarations

Ethics approval: Not applicable.
Consent to participate: Not applicable.
Consent to publication: Not applicable.
Competing interests: The authors declare no competing interests.
Funding: Not applicable.
Data availability: The paper has no associated data.

References

[1] F. Wang, X. Yan, C. Zhang, L. Deng, Y. Lu, M. Nastasi, et al., Fundamental mechanisms of laser shock processing of metals and ceramics. Proceedings Volume 10813: Advanced Laser Processing and Manufacturing II, 2018. Nov.

[2] A. Gill, A. Telang, S. Mannava, D. Qian, Y.-S. Pyoun, H. Soyama and V.K. Vasudevan, Comparison of mechanisms of advanced mechanical surface treatments in nickel-based superalloy. Materials Science and Engineering: A, 2013. 576: p. 346-355.

[3] K.R. Kuveya, C. Polese, M. Newby and D. Glaser, Laser peening without coating versus shot peening effects on residual stress and surface modification of X12CrNiMo12 turbine blade. 6th International Conference on Laser Peening and Related Phenomena, 2016. Nov.

[4] M. Mahoney, LSP Technologies, Inc. Laser Peening Cell Now at ZAL in Hamburg [Online]. Available from: https://www.lsptechnologies.com/laser-peening-cell-now-at-zal-in-hamburg/, 2018.

[5] E. Hoffman, LSP Technologies, Inc. Laser Peening: Who? What? Where? When? Why? [Online]. Available from: https://www.lsptechnologies.com/laser-shock-peening-who-what-where-when-why/, 2017.

[6] R. Zhu, Y.K. Zhang, G.F. Sun, S.B. Zhang, P. Li and Z.H. Ni, Finite element analysis of residual stress induced by multiple laser shock peening with square spots. International Journal of Peening Science and Technology, 2018. (1): p. 99-118.

[7] D. Armfield, Optimised implementation of physics-based strain-rate dependent material models for the improved simulation of the laser shock peening process. 2018, University of Pretoria.

[8] K. Ding and L. Ye, Laser shock peening: performance and process simulation. 2006: Woodhead Publishing.

[9] K. Kulkarni, Experimental characterization and finite element simulation of laser shock peening induced surface residual stresses using nanoindentation. 2012. MSc. thesis, University of Cincinnati.

[10] M. Sticchi, P. Staron, Y. Sano, M. Meixer, M. Klaus, J. Rebelo-Kornmeier, et al., A parametric study of laser spot size and coverage on the laser shock peening induced residual stress in thin aluminium samples. The Journal of Engineering, 2015. (13): p. 1-9.

[11] R. Sundar, P. Ganesh, R.M. Gupta, G. Ragvendra, B.K. Plant, V. Kain, et al., Laser shock peening and its applications: A review. Lasers in Manufacturing and Materials Processing, 2019. 6(7): p. 424-463.

[12] H. Kamkarrad, High repetition rate laser shock peening on biodegradable magnesium alloys. 2016. PhD. thesis, Concordia University.

[13] B. Banerjee, The mechanical threshold stress model for various tempers of AISI 4340 steel. International Journal of Solids and Structures, 2007. 44(3-4):834-859.

[14] P.S. Follansbee and U.F. Kocks, A constitutive description of the deformation of copper based on the use of the mechanical threshold stress as an internal state variable. Acta Metallurgica, 1988. 36(1):81-93.

[15] G.J. Jansen Van Rensburg and S. Kok, Tutorial on state variable based plasticity: An ABAQUS UHARD subroutine. In: Eighth South African Conference on Computational and Applied Mechanics, Johannesburg, South Africa, 2012. 3−5 September.

[16] D.M. Goto, J.F. Bingert, S.R. Chen, G.T. Gray and R.K. Garrett, The mechanical threshold stress constitutive-strength model description of HY-100 steel. Metallurgical and Materials Transactions A, 2000. 31(8):1985-1996.

[17] C.C. Engebretsen, Laser shock peening pressure impulse determination via empirical data-matching with optimization software. 2020, PhD. thesis, Air Force Institute of Technology.

[18] N. Hfaiedh, P. Peyre, H. Song, I. Popa, V. Ji and V. Vignal, Finite element analysis of laser shock peening of 2050-T8 aluminum alloy. International Journal of Fatigue, 2015. 70: p. 480-489.

[19] S. Glen, M. Gaultieri and E. Rothberg, Mathematical optimization + ML: Featuring Forrester survey insights, 2019. [Video]. Portland: Gurobi Optimization.

[20] SIMULIA, Cost of mesh refinement in implicit and explicit analyses [Online]. Available from: https: https://abaqus-docs.mit.edu/2017/English/SIMACAEGSARefMap/simagsa-c-abscostmeshref.htm.

[21] R.E. Munoz, Finite element modelling (including material grain fefinement prediction) when turning advanced aerospace alloys. 2014, PhD. thesis, The University of Birmingham, Birmingham, England.

[22] G. Singh, Effective simulation and optimization of a laser peening process. 2009, PhD. thesis, Wright State University, Dayton, Ohio.